

Trapping and Imaging of Ultracold Erbium Atoms

Eugene Kim

Project Number: A&L06

Supervisor: Professor Robert Smith

ABSTRACT

We report on progress towards the study of ultracold erbium atoms in a quasi-2D homogenous "pancake" trap. In particular, we describe the design and implementation of a circular box trap using repulsive (blue-detuned) light modulated by a phase-only Spatial Light Modulator (SLM). Combining this with an attractive (red-detuned) sheet beam forms a tunable pancake-shaped trap suitable for the study of a variety of fields such as exotic supersolid states, non-equilibria phase transitions, and polaron physics. After optimisation of the optical setup and SLM hologram parameters, we generate a box trap with a fitted power law exponent of 18.1 and a trap depth of $2.15\mu\text{K}$ with angular uniformity range $\pm 23\%$. The current trapping system generates a $0.19\mu\text{K}$ trap depth per 1mW of trapping beam incident on the SLM and is open to further optimisation.

Furthermore, we describe the development of an imaging system and camera software that enables the imaging of erbium atoms in this pancake trap. The imaging system provides a magnification of 3.0 ± 0.5 and has a diffraction-limited spot size of $0.72\mu\text{m}$ upon the camera. Finally, we demonstrate a proof-of-concept implementation of our absorption imaging and box-trapping system by imaging 8,300 trapped erbium atoms - a figure that, while significantly lower than the anticipated 10^7 , offers valuable insights for future optimisation efforts and the potential for substantially improved quality of pancake traps.

1 INTRODUCTION

Ultracold Gases research is interesting for two reasons. Firstly, ultracold gases have enabled the design of experiments investigating a variety of fields. These include and are not limited to Bose-Einstein Condensates (BECs), Fermi gases, many-body systems, spin dynamics, non-Markovian dynamics, BCS theory, superfluidity, non-equilibria phase transitions, Roton physics, quantum magnetism, and impurity physics.[1][2] Secondly, ultracold gases and the techniques developed to manipulate them have also been wielded for a range of related technologies. For instance, ultracold gases have enabled the world's most accurate atomic clocks to deliver precise GPS, transform telecommunications, and innovate scientific research. Ultracold gases offer a uniquely controllable and versatile platform, making it both a thriving area of physics research and a technological driver.[3]

One particularly excellent candidate for ultracold gases research is erbium, a lanthanide with atomic number $Z = 68$. Firstly, erbium has a ground state with a large effective moment $\mu_z = m_J g_J \mu_B \approx$

$7\mu_B$, opening doors to exploring and tuning systems with strong magnetic dipole-dipole interactions. Secondly, erbium's rich electronic structure greatly favours laser cooling, optical trapping, and absorption imaging. Of particular interest is the blue **401nm** radiative transition. This transition is a very prominent one, thus causing erbium to exhibit a high photon scattering rate making it ideal for effective absorption imaging. Furthermore, blue light wavelengths near 401nm exerts a leading order influence on the atomic polarisability α , also making optical trapping using 372nm convenient.

Recent developments in the shaping of optical trapping potentials have opened many possibilities within ultracold gases research. One increasingly popular trapping geometry is the uniform (flat-bottom) optical box trap, contrasting the commonly used harmonic or Gaussian ones. Trapping quantum gases in homogeneous geometries has the powerful advantage of easing the interpretation of results and their comparison with theory more directly. Furthermore, uniform potentials create the unique opportunity to investigate qualitatively new experiments probing highly density-sensitive effects like

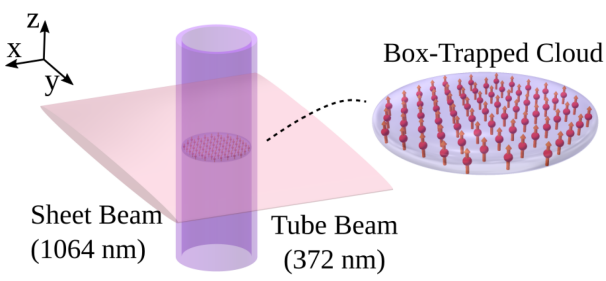


Figure 1: The homogenous optical box trap, also known as the “pancake” trap. The first part of the project focuses on the implementation of the blue-detuned 372nm tube beam. Image credits to L. Hofer (2023) [4].

the polaron energy shift. While box traps have been implemented successfully for alkali atoms like potassium, this has never been done for strongly dipolar atoms like erbium.[5]

Here, we report two key steps taken towards the realisation of an experimental setup to study ultracold dipolar erbium atoms in a quasi-2D homogeneous “pancake” trap.

Firstly, using a Spatial Light Modulator (SLM), we have realised a hollow and cylindrical 372nm blue-detuned repulsive beam. This “tube” beam, when combined with an existing red-detuned attractive sheet beam, creates the desired quasi-2D pancake trap that displays both strong anisotropy and homogeneity in the radial direction, as shown in Figure 1. The resultant box trap promisingly produces a fitted power law exponent of 18.1, a trap depth of $2.15\mu\text{K}$, and a small, random floor noise averaging $0.018\mu\text{K}$.

Secondly, we have designed, built, aligned, and characterised an optical absorption imaging system. By mounting optical components and integrating a new camera with the wider lab software, we utilised absorption imaging to image the high-quality pancake traps. Furthermore, we have imaged a proof-of-concept implementation of box-trap containing a calculated 8,300 erbium atoms.

The rest of the report is organised as follows. In Chapter 2 we provide an overview of the experimental setup, both from a broad perspective of the erbium machine, and from a focused overview of the optics used for trapping and imaging atoms in the Science Cell (SC). In Chapter 3 we focus on the trapping system, explaining the physics behind optical dipole traps, illustrating the use of SLMs, exploring the engineered optical setup, and finally char-

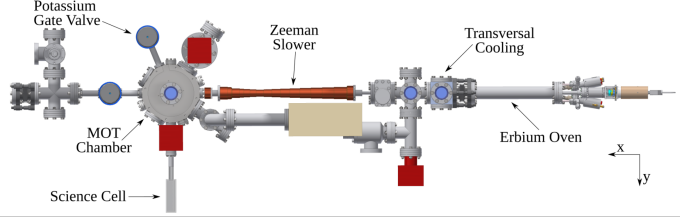


Figure 2: Overview of the erbium machine components. Image credits to M. Krstajic (2021) [6].

acterising the tube-shaped optical potential. Then, in Chapter 4, we focus on the imaging setup, elucidating upon the absorption imaging technique, as well as the alignment tools used to optimise our system. Finally, we conclude with Chapter 5 where we summarise what has been achieved throughout the project and evaluate what remains to be done.

2 EXPERIMENT OVERVIEW

2.1 Wider Setup

The erbium machine forms the core of the wider experimental architecture, and its main function is to prepare the ultracold erbium BEC atoms. Visualised in Figure 2, the erbium machine consists of the following stages:

1. **Effusion Cell Oven:** Heats the atomic sample to $1,100^\circ\text{C}$, initiating the release of atoms.
2. **Transversal Cooling and Zeeman Slower:** Doppler cools atoms from up to $\sim 1,100\text{K}$ (350m/s) down to $< 670\text{mK}$ (10m/s).
3. **Magneto-Optical Trap (MOT):** Doppler and Sisyphus cools; further cooling achieved by compressed MOT (cMOT) where atoms are cooled to $10\mu\text{K}$ (4cm/s).
4. **Optical Dipole Trap (ODT):** Evaporatively cools and transports the erbium atoms into the Science Cell using red-detuned attractive 1030nm light.
5. **Science Cell (SC):** Contains the atoms to be pancake-trapped and absorption-imaged. By slowly reducing trap depth, additional evaporative cooling to quantum degeneracy at $\sim 100\text{nK}$ is achieved.

On a typical experimental run, the Science Cell (SC) contains around 10^7 erbium atoms at the coldest part of their journey, ready to be pancake-trapped and absorption-imaged. The SC itself is a 2mm-thick ultra-high vacuum (UHV) N-BK7 glass

chamber and is surrounded by several components. This includes, of course, the pancake trap and absorption imaging optics, but also the ODT transport beam optics as well as two pairs of large Helmholtz coils that tune the interparticle contact and dipole-dipole interactions, which in turn determine what kind of physics is researched.

2.2 Trapping and Imaging System

Trapping & Imaging Optical Setup

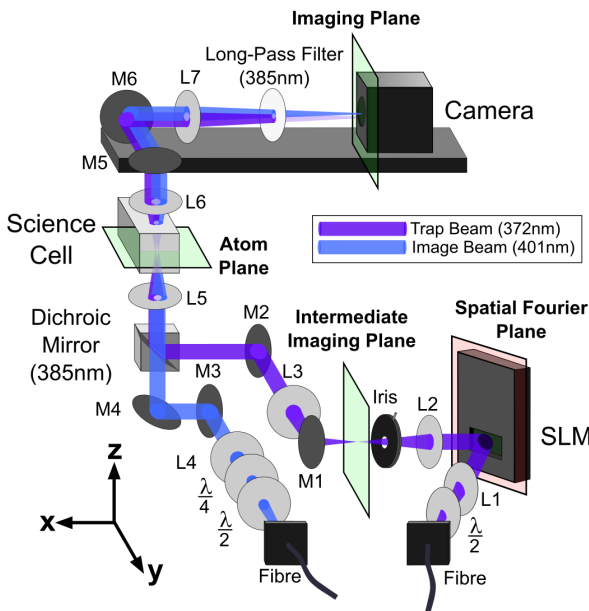


Figure 3: 3D Model Overview of the Tube Trapping and Absorption Imaging Setup. The three green planes represent the **Focal Planes** of the trapping and imaging beams. The red plane represents the **Spatial Fourier Plane**, where the SLM generates its holograms. Further details including the focal lengths of lenses are provided in the 2D Models in Sections 3.3.2 and 4.2.

The combined trapping and imaging setup is shown in Figure 3. The 372nm trapping beam and the 401nm imaging beam join optical paths after reflecting off of or transmitting through Newport's 10CGA-385 **dichroic mirror**. This is a mirror that only reflects wavelengths below 385nm and transmits all other wavelengths. The two aligned beams propagate through the rest of the optical system, focusing first into the Atom Plane and then finally into the imaging focal plane at the camera retina. Measurements of the 50mm and 150mm lenses' positions (L6 and L7 in Figure 3) provide an optical magnification between the SC and the camera of

3.0 ± 0.5 , where the errors propagate from the errors in the lenses' position measurements.

As alluded to in Section 2.1, there are several spatial constraints to consider. Firstly, there exist several competing experimental components near the SC. We efficiently utilised the available space by combining the optical paths of the 372nm trapping and 401nm imaging beams, both aligned with the vertical z-axis by using a dichroic mirror at a 45-degree angle to each beam. Secondly, anticipating future rearrangements of the experiment's architecture, we place the trapping and imaging optics as far as possible from the science cell without compromising beam resolution. Lastly, we installed two additional mirrors at approximately 45 degrees to each beam path to achieve both fine-tuning of angles and efficient use of gaps between other components.

To prepare the trapping and imaging beams, we utilise M Squared SolsTiS lasers and custom-designed **Acousto-Optic Modulators (AOMs)**. AOMs are powerful techniques as they allow us to tune both the intensity and frequency of a laser beam without directly changing the parameters of the laser generating apparatus (like the dimensions of the cavity or the material of the gain medium).

3 CREATING AN OPTICAL BOX TRAP

In this section, we explore the core aspects of implementing an optical box trap: the physical principles behind optical dipole traps, the mechanisms of the Spatial Light Modulator, the trapping optical setup, and the characterisation of the optical potential.

3.1 Optical Dipole Traps

Optical Dipole Traps (ODTs) are optical potentials created by the interaction between light and atoms. The light's complexified electric field $\mathbf{E} = \mathbf{E}_0 e^{i\omega t}$ induces electric dipole moments $\mathbf{p} = \alpha \mathbf{E} = \alpha \mathbf{E}_0 e^{i\omega t}$ in atoms with polarisability α . Note that \mathbf{E} , \mathbf{p} , and α are all represented by complex quantities, the real parts of which ($\text{Re}(\mathbf{E})$, etc.) are the actual physical quantities.

The **magnitude** of the trapping potential is controlled via the average intensity $I = \frac{1}{2}c\epsilon_0 E_0^2$ because the interaction energy density is:

$$\langle U \rangle = -\langle \mathbf{p} \cdot \mathbf{E} \rangle = -\frac{\text{Re}(\alpha)I}{\epsilon_0 c}. \quad (1)$$

Furthermore, we can also change whether the in-

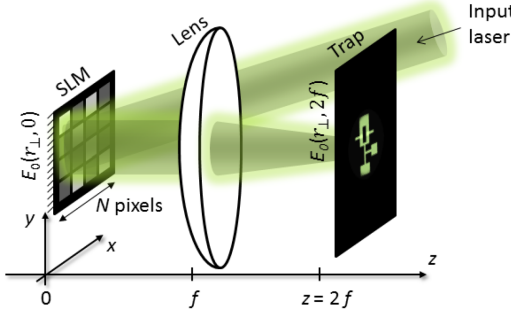


Figure 4: Optics for producing holograms using an SLM.

teraction potential is **repulsive** or **attractive** by changing its sign. We do this by using an appropriate laser detuning $\delta = \omega - \omega_0$, where ω_0 is a specific and prominent radiative transition frequency of the BEC atoms. This can be seen under a simplified Lorentz oscillator model, where for small detunings δ , $\text{Re}(\alpha) \propto \frac{\delta}{\delta^2 + \Gamma^2/4}$.

Thus, generally speaking, a **blue-detuned** laser induces negative polarisability to create a repulsive electric field gradient, and a **red-detuned** beam a positive polarisability to create an attractive one. In reality, the total atomic polarisabilities of dipolar atoms like erbium have many other contributions, which can complicate the optical trapping scheme. Fortunately, erbium has desireable polarisabilities at 372nm, with a negative polarisability of -779 a.u., and at 1030nm, with a positive polarisability of 178 a.u., where 1 atomic unit (a.u.) = $4\pi\epsilon_0 a_0^3 = 1.65 \times 10^{-41} \text{C}^2 \text{m}^2 \text{J}^{-1}$, thus allowing the successful implementation of the pancake trap [6].

3.2 Spatial Light Modulators

To create an optical box trap, we utilise a **Spatial Light Modulator** (SLM), one of the most effective technologies for creating customised trapping potentials. This follows similar successful approaches seen with trapping alkali atoms [7][8].

3.2.1 How Do SLMs Work?

SLMs are devices with 2D surfaces that can be programmed on a pixel-by-pixel level to modulate the amplitude, phase, and polarisation of incident light, the exact combination depending on the specific device. Light modulation at a single hologram plane constructs the desired beam pattern at the far-field diffraction plane. If the trapping optics setup

Shape	Hologram	Theoretical diffraction pattern	Experiment
Circle (pseudo-LG)	$\phi = \ell\theta$		Circle of radius $\sim 0.5\ell$ ($\ell \gg 1$)
Circle (axicon)	$\phi = \frac{kR}{f} r_\perp$		Circle of radius R

Figure 5: Summary of the properties of pseudo-Laguerre-Gauss (pLG) and Spiral Axicon (SA) beam properties, as well as a comparison between their theoretical and experimental implementations. [7].

is modelled as effectively a single lens of focal length f , then the far-field diffraction pattern is brought in from infinity to a trapping plane at $z = 2f$, as shown in Figure 4. We have chosen to use a **phase-only** SLM which only modulates the laser's phase and not the amplitude of the incident light. This ensures we do not block out any of the incident light via amplitude modulation, thus producing the desired deep atom traps with lasers of reasonable power.

The hologram plane is the physical representation of the **spatial Fourier plane**. To see this mathematically, we consider a beam of the form $U_i(x, y)$ incident upon the SLM, whose hologram pattern is modulated by a phase pattern $\phi(x, y)$. Given the beam's wavevector $k = 2\pi/\lambda$, Fraunhofer diffraction theory allows us to find the output $U_o(x', y')$ as proportional to the spatial Fourier Transform of the modulated input beam:

$$\propto \int_{-\infty}^{\infty} \int_{-\infty}^{\infty} U_i(x, y) e^{i\phi(x, y)} e^{\frac{-ik}{2f}(xx' + yy')} dx dy. \quad (2)$$

After modulation, the exiting light diffracts into different output orders (0th, 1st, 2nd, etc.). Crucially, we **iris** out the 0th order light and instead use the 1st order. This is because all SLMs have sub-unity **fill factor**, which is the proportion of each pixel area that successfully modulates. This means that there will always be some non-modulated component within the 0th order beam destructively interfering with its modulated components. Therefore, the utilisation of the 1st order beam as the trapping potential is optimal because this ensures both that all the light is modulated and that the non-zeroth order beam with the greatest intensity is used.[4]

3.2.2 Tube Trap Hologram

Many different holograms can be used to generate the circular tube beams. We carefully consider the suitability of two tube-beam hologram candidates.

The **pseudo-Laguerre-Gauss (pLG)** beam is created by a spiral phase winding hologram $\phi = l\theta$ parameterised by the winding number l . Alternative holograms exist, and one worth noting is the **Spiral-Axicon (SA)**, which is a linear combination of the pLG hologram and a radial phase gradient called the Axicon $\phi = \frac{kR}{f}r_\perp$.

Past experimental implementations of both pLG and SA tube traps, as shown in Figure 5, demonstrates clear trade-offs between the use of the two holograms. SA traps tend to generate steeper trap walls and offer greater trap depths for a given total trap beam power incident on the SLM. However, the SA suffers from non-random noise structures in the flat region of the box trap, which is far less preferable to the random noise generated by pLG traps due to its stronger unwanted effects on the overall trap geometry. [7] [9] Thus, this project focuses on optimising a pLG trap.

To find analytical solutions to the beams generated by pLG holograms, consider an incident Gaussian electric field $E_{LG}(\mathbf{r}_\perp, z = 0) \propto \frac{w_0}{w} e^{(-r_\perp^2/w^2)}$ illuminates the SLM, where w is the waist size and $w_0 = \lambda f / \pi \omega$ is the diffraction-limited spot size in the spatial Fourier plane. Using Equation 2:

$$E_{LG}(\mathbf{r}_\perp, z = 2f) \propto \frac{r_\perp}{w_0} e^{(-r_\perp^2/2w_0^2)} \left[I_{\frac{l-1}{2}} \left(\frac{r_\perp^2}{2w_0^2} \right) - I_{\frac{l+1}{2}} \left(\frac{r_\perp^2}{2w_0^2} \right) \right] e^{(il\theta)}. \quad (3)$$

where $I_n(z)$ is a modified Bessel function of the first kind. Numerical analysis of Equation 3 demonstrates that the pLG beam's radius is $r \approx l\omega_0/2$ and an innermost ring thickness of $\delta r \approx 0.35l\omega_0$. [7]

3.3 Optical Setup for Tube Beam Generation

In this section, we outline the optical setup implemented for the generation of the blue-detuned tube beam.

3.3.1 The SLM Device

We utilise the Hamamatsu X13267-05 LCOS-SLM, which is a reflective, phase-only SLM based on Liquid-Crystal-On-Silicon (LCOS) technology. This

contains an **active area** of 9.9mm x 7.5mm of 792 x 600 liquid crystal with **pixel size** (length) 12.5 μm . The SLM is quoted to have a **threshold power** of 15mW over the entire active area, and thus a **threshold intensity** of 202 W m⁻², with an active lifetime of 10,000 hours. It is quoted to have a fill factor of 0.96, and a preferred horizontal polarisation.

The SLM has 256 Analogue-to-Digital Conversion (ADC) voltage values, ranging from 0 to 255, but this does not directly map to a phase modulation of 0-2 π for two reasons. Firstly, our SLM screen is not perfectly uniform and has irregularities on a per-pixel basis. We correct for these systematic errors by utilising Hamamatsu's device-specific calibration files. Secondly, the actual phase modulation achieved depends on the light's wavelength. Hamamatsu only supplies wavelength-dependent calibration files for wavelengths of 400nm, 410nm, and 420nm. Past work quadratically extrapolates from these three files to generate the appropriate calibration file and to calculate an adjusted ADC level range from 0 to 199 for 372nm incident light.[9]

3.3.2 Tube Trapping Optics Setup

The tube trapping optical system is illustrated in Figure 6. First, the trapping beam is carried into the optical system through a Schäfter+Kirchhoff APC.EC-700-P optical fibre, which is a polarization-maintaining single-mode fiber cable with a Gaussian intensity distribution and a maximum power output of 70 mW. The light emerging from the fibre has a numerical aperture of NA = 0.08.

The trapping beam is passed through a half-waveplate to ensure that its polarisation is set to the SLM's preferred horizontal polarisation for phase modulation. Then, the beam is collimated by a 75mm lens onto the SLM screen with incident diameter $\approx 2d \times NA = 12\text{mm}$, which is large enough to cover the 9.9mm x 7.5mm active region of the SLM, but small enough to prevent clipping by the 16mm x 12mm SLM screen entrance hole. A 26 degree angle is set between the incident light and the SLM as past research experimentally demonstrated that this angle maximised the 1st order efficiency for 372nm beams when tested in conjunction with the SLM's adjusted ADC level range from 0 to 199 [9]. The SLM's ADC level adjustment is further explained in Section 3.3.1.

The SLM beam then passes through a 2f lens system: a pair of 200mm lenses 400mm apart (L2

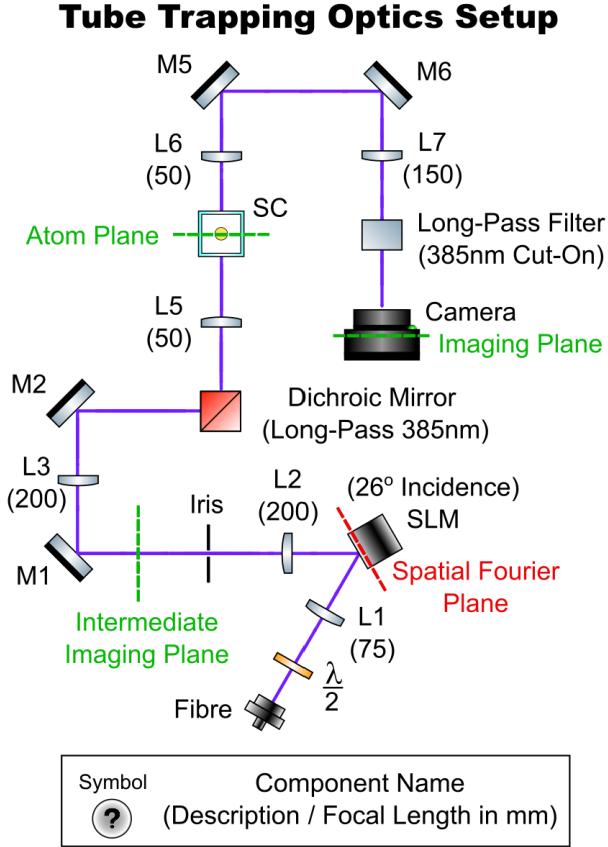


Figure 6: 2D Drawing of the Tube Trapping Optics System. The same labelling of the component names has been used for consistency.

and L3 in Figure 6). This is done for two reasons. Firstly, this opens up access to an additional “intermediate imaging plane” at the focal point halfway between the two lenses, allowing us to analyse the trap and triangulate any potential misalignment thus far in the trapping beam’s propagation. Secondly, this allows the fitting of an adjustable iris diaphragm near the intermediate imaging plane to block out the SLM’s 0th order light, selectively permitting its 1st order light through instead. The SLM’s diffraction beams are also further explained in Section 3.3.1.

3.4 Characterisation of the Optical Potential

Python code and integrating it with the lab’s SQL database, we programme holograms onto the SLM to generate pLG tube traps across a number of hologram variables. Upon a few iterations of optimisation for winding number $l = 20$, we found the hologram with the greatest overall trap quality to have a

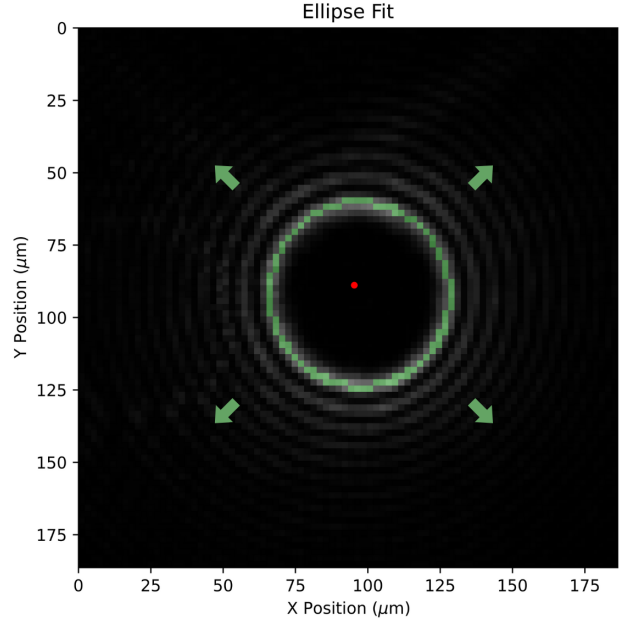


Figure 7: Ellipse of 1 pixel thickness fitted onto the peak of the pLG tube trap. The red dot is the user’s specified initial guess of the ellipse fit’s central point. By scaling its semi-major and semi-minor axes, the ellipse becomes a “scanner” through which we create a radial profile, as seen in Figure 8.

virtual cylindrical Fresnel lens of focal length 18mm at an angle 18° , a hologram centre-point translation offset of $x = 0$ and $y = -50$, with an additional virtual circular Fresnel lens of focal length $F = -50$ mm.

The image analysis code works by first fitting an ellipse onto the trap image. This requires an initial guess of the ellipse parameters. This is provided by a user-specified centre point (x_0, y_0) , from which we guess the ellipse’s semi-major and minor axes a and b from the distance to the brightest image pixel. We lack information on the angular rotation θ , so leave its guess to zero. Furthermore, we force the thickness of the ellipse to equal 1 pixel. This fitted ellipse, as shown in Figure 7, is then used as a mask or a “scanner” over which we determine the values of five key metrics assessing the efficacy of our circular box-trap.

3.4.1 Metric 1: Eccentricity

Having found the semi-major and semi-minor axes $a = 31.8\mu K$ and $b = 31.0\mu K$ from the ellipse fit, we find that the eccentricity is $e = \sqrt{1 - (b/a)^2} = 0.226$. While this represents a non-negligible distortion, this can be corrected for by implementing a

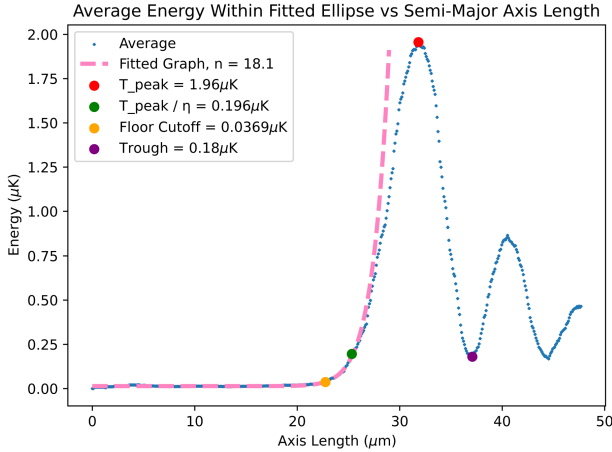


Figure 8: Radial Profile of a Tube Trap.

virtual cylindrical Fresnel lens with a smaller focal length through the SLM hologram.

3.4.2 Metric 2: Radial Steepness

Homogeneous box traps ideally have infinitely steep potential walls; in reality, an optical trap wall’s steepness is finite. This is due to the non-zero diffraction of real optical systems as well as the SLM’s inherent limitations from pixellation effects and systematic errors unaccounted for in the extrapolated calibration for 372nm wavelengths.

To assess the steepness of the trap wall, we create a radial profile of the trap using the average intensity “scanned” by an ellipse scaled across a range of semi-major axis lengths, as shown in Figure 8. Fitting a power law $I(r_\perp) \propto r_\perp^n$ onto the radial profile provides an optimised fit of $n = 18.1$. The power law is fitted to the trap region only where the bulk majority of the atoms will explore: areas with energies from 0 to $\sim k_B T$, shown by the pink dotted line in Figure 8. Parameterising the trap depth by η such that $U_{\text{peak}} = \eta k_B T$, we ensure sufficient trapping beam intensities such that $\eta \sim 10 \gg 1$ to minimise the loss rate of the high energy tail of trapped atoms.

3.4.3 Metric 3: Angular Uniformity

The innermost “ring” of the trap peak should ideally be perfectly circular, ensuring complete rotational symmetry of the box trap. In reality, there will always be asymmetries around the ring.

We assess the trap’s angular homogeneity by creating an angular profile of the ellipse fitted to the trap peak. The true maximum of the trap wall height is found at each point along the ellipse by finding the

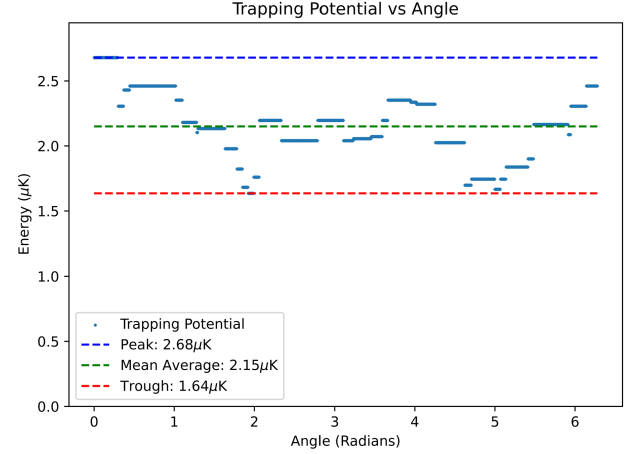


Figure 9: Angular Profile at Average Ellipse Energy U_{peak}/η .

maximum power within a 3 pixels x 3 pixels box centred at the ellipse point. Finding the mean of these local maxima provides a more reliable measure of the trap depth of $2.15\mu K$ than simply using the peak thermal energy found in the radial profile in Figure 8.

We find that the maximum trap height is $2.68\mu K$ and the minimum is $1.64\mu K$ with a half-range of $0.50\mu K$. Thus, the pLG beam’s trap depth is uniform to within around $\pm 23\%$.

3.4.4 Metric 4: Floor Uniformity

While a box trap should ideally have zero potential in the “floor” between its walls, there will always be a certain level of noise, as exemplified by Figure 10. The floor noise can originate from random fluctuations and non-random sources like aperture fringe patterns and SLM pixellation effects. As reasoned in section 3.2.2, a random noise distribution is preferable to a non-random one because random distortions to the overall trap geometry will have, on average, only asymmetries at a microscopic level.

We define the floor cut-off point to be at the trap potential’s rising point of inflection, where the second-order differentials between neighbouring points rises above zero. To quantify the floor noise and its structure, we isolate the floor’s non-zero values, as shown in Figure 10, and search for Spearman correlations between the floor noise and the transversal, radial, and angular directions. The Spearman rank correlation coefficient measures the strength and direction of the monotonic relationship between two ranked variables. Unlike the Pearson correlation coefficient, which only assesses linear re-

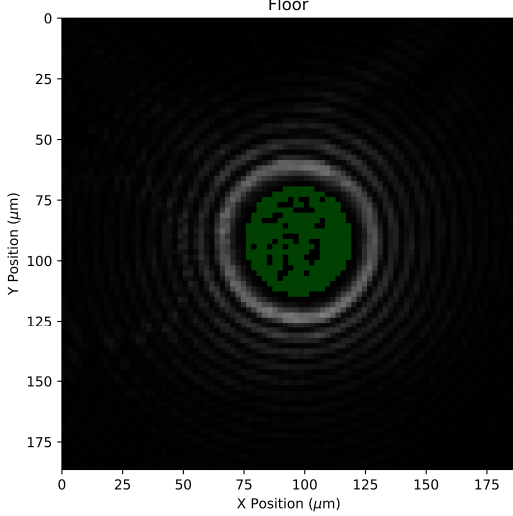


Figure 10: Image of Trap Floor, where non-zero value pixels within the floor are all highlighted in green with the same pixel value of 1.

relationships, the Spearman correlation test does not assume that the relationship between the variables is linear. The average non-zero floor noise is a negligible $0.018\mu\text{K}$ which is less than 1% of the trap depth; the only statistically significant Spearman correlation is a small -0.06 in the radial direction with p-value 2.14×10^{-7} . This shows there is a small tendency for floor noise to gather around the centre.

3.4.5 Metric 5: Energy Efficiency

There remain many sources of inefficiencies in the conversion of incident power into a trapping potential. Firstly, there are losses into other SLM-diffracted beam orders: given a 11.5mW beam incident upon the SLM, a power meter measurement reveals that only 5.3mW survives into the 1st order, (an efficiency of 46%). Secondly, and more concerningly, only 2.3% of the 1st order beam power is transferred into the inner “ring” of the pLG trap beam; the rest is lost into its outer “rings”. This provides a total efficiency of a meagre 1.1%.

This result is not, however, inherently problematic. Given a trap depth of $2.15\mu\text{K}$ and input power of 11.5mW incident on the SLM, the pLG trap has a power-to-depth conversion rate of $0.19\mu\text{K}/\text{mW}$. This is barely high enough to trap atoms with temperatures $\sim 100n\text{K}$. With further optimisation of the pLG hologram parameters and the optical setup, it seems likely that a pLG beam will effectively trap ultracold erbium atoms in the Science Cell.

3.4.6 From Pixels to Intensities & Energies

To relate pixel values and pixel indices to real beam power/intensity/energy and spatial positions within the SC, we found the number of photons incident upon each camera pixel $N = \text{CF} \times (V_{\text{out}} - V_{\text{off}})/\text{QE}(\lambda)$, where CF is the conversion factor between electrons freed per photon count, and V_{out} and V_{off} are the 16-bit pixel value for the image and the dark background respectively. The Quantum Efficiency $\text{QE}(\lambda)$ is the average probability of capturing an incident photon, for which at $\lambda = 372\text{nm}$, the Hamamatsu camera quotes a QE of 0.461, and for fast scans, a CF of 0.21.

The power captured per pixel is $P = Nhc/\lambda T$, where the exposure time $T = 300\mu\text{s}$. Furthermore, each pixel in the camera images a real cross-sectional area A within the science cell. This is related to the width of each pixel $W_{\text{pixel}} = 6.5\mu\text{m}$, the magnification of the optical system $M_{\text{optical}} = 3.0 \pm 0.5$, and the UV Filter attenuation factor $F_{\text{filter}} \approx 10^{-5}$ by the following:

$$A_{\text{SC}} = F_{\text{filter}} \left(\frac{W_{\text{pixel}}}{M_{\text{optical}}} \right)^2. \quad (4)$$

Thus, the corresponding light intensity at the Science Cell is $I_{\text{SC}} = P_{\text{pixel}}/A_{\text{SC}}$. For trapping beams, this intensity can be substituted into Eq. 1 to find the interaction potential energy. Dividing this by the Boltzmann constant k_B provides the thermal energy T_{th} in units Kelvin.

4 ABSORPTION IMAGING OF ULTRACOLD ERBIUM

4.1 Absorption Imaging

We utilise absorption imaging methods for the optical imaging of ultracold atoms. Absorption imaging works by illuminating a 401nm resonant laser beam onto the atoms and imaging the “shadow” created within the beam. This can be used to determine the atom density and temperature. Absorption imaging analysis requires three distinct images:

1. **Background Image I_b :** Taken **without** any probe light or atomic cloud.
2. **Probe Image I_p :** Taken **with** the probe beam but **without** the atomic cloud.
3. **Atom Image I_a :** Taken **with both** the atomic cloud and probe light.

The optical density (OD) of the image attenuates the probe beam intensity as $I(\omega, x, y) =$

$I_0(x, y)e^{-\text{OD}(\omega, x, y)}$. Using the three images we can calculate the OD:

$$\text{OD}(\omega, x, y) = \log \left(\frac{I_p - I_b}{I_a - I_b} \right) \quad (5)$$

This can help us find the number density of atoms $n(x, y, z)$ because $\text{OD}(\omega, x, y) \equiv \int \sigma(\omega) n(x, y, z) dz$, where the optical cross-section $\sigma(\omega)$ is given by:

$$\sigma(\omega) = \frac{3\lambda^2}{2\pi} \frac{1}{1 + 4\left(\frac{\delta}{\Gamma}\right) + \frac{I_0}{I_{\text{sat}}}} \approx \frac{3\lambda^2}{2\pi}. \quad (6)$$

The approximation on the right is valid under low, unsaturated light intensities ($I_0 \ll I_{\text{sat}}$) and near-resonant transitions ($\delta = 0$). For erbium's 401nm transition, $I_{\text{sat}} = 60\text{mW/cm}^2$.[4]

If the pancake trap is being used, prior to capturing the atom image the pancake trapping potential is abruptly deactivated, allowing the gas to expand freely. Turning off the trap is a common and important technique in ultracold gases imaging because the expansion lowers the OD to measurable values whilst concurrently expanding the atom clouds to sizes above the imaging resolution.

4.2 Optical Setup for Absorption Imaging

Here we focus on the imaging part of the setup, as can be seen in detail in Figure 11.

Upon exit from the fibre, the imaging beam propagates through a half-wave plate and a quarter-wave plate. This ensures the generation circularly polarised light to drive the 401nm transition (J, m_J): $(6, -6) \rightarrow (7, -7)$. Once collimated by a 75mm lens, it joins optical paths with the trapping beam at the dichroic mirror and propagates through the same system discussed in Section 4.2. The imaging beam focuses onto the imaging plane. This is where the Hamamatsu C14440-20UP Orca-Fusion camera sits, a CMOS sensor camera with 2304×2304 pixels of width $6.5\mu\text{m}$.

With the pancake box trap turned off, we ensure alignment between different parts of the imaging system. First, we optimise alignment between the imaging beam with the camera by ensuring that the imaging beam is centred, in focus, and minimally distorted. We further optimise alignment between the imaging beam and the Science Cell atoms trapped in the harmonic ODT transport beam by minimising the residuals of the Gaussian fit applied to the OD profile. The images taken using this alignment process is shown in 12. We expect such a Gaus-

Absorption Imaging Optics Setup

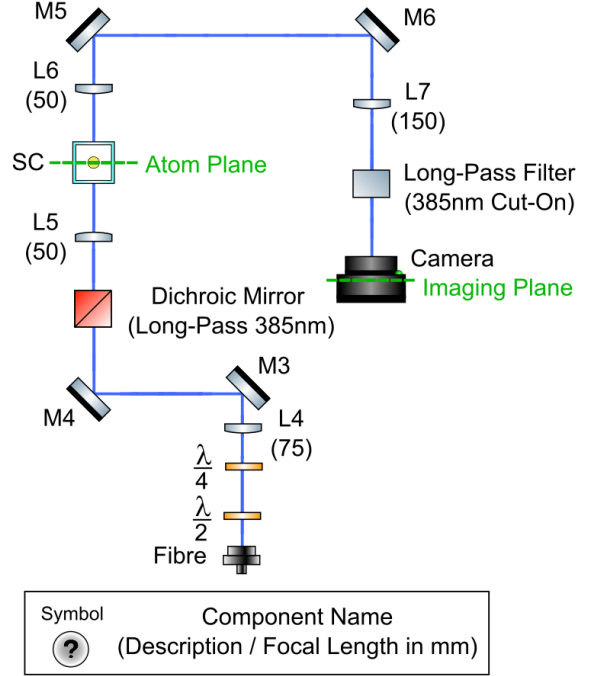


Figure 11: 2D Drawing of the Absorption Imaging Optics System. The same labelling of the component names has been used for consistency.

sian distribution of atom number density for a thermal gas (not cold enough to be a BEC), because a harmonic trap potential $E = \sum_{n=1}^3 \frac{1}{2} M \omega_{x_n}^2 x_n^2$ causes the Boltzmann distribution of atom population to become a Gaussian along each axis: $e^{-\frac{E}{k_B T}} = \prod_{n=1}^3 e^{-\frac{1}{2} M \omega_{x_n}^2 x_n^2 / k_B T}$. The long “cigar” shape of the atoms along y-axis of the Science Cell comes from the fact that $\omega_y \ll \omega_x, \omega_z$. [10]

4.3 Box-Trapped Erbium Atoms

Erbium atoms have been successfully box-trapped, and is shown in Figure 13. We find an average non-zero OD of around 0.51. Using Eq. 6, this gives us an average cross-sectional atom number density $n(x, y) \equiv \int n(x, y, z) dz = 6.6 \times 10^{12} \text{m}^{-2}$. Approximating the circle of atoms with radius $20\mu\text{m}$ gives an area of 1.2×10^{-9} . Thus, the box-trap contains around 8,300 atoms.

This falls substantially short of the theoretically expected 10^7 erbium atoms in the SC. This is due to the many sources of loss during the heating, cooling, transport, and trapping stages of the erbium machine. A particularly large loss of atoms is to be expected from the fact that a non-optimised tube trap was used for the result in Figure 13. It was not pos-

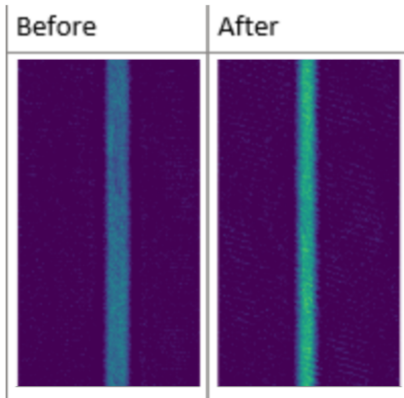


Figure 12: Calibration of the Imaging Optics. Final fit width of Gaussian = 1.23×10^5 .

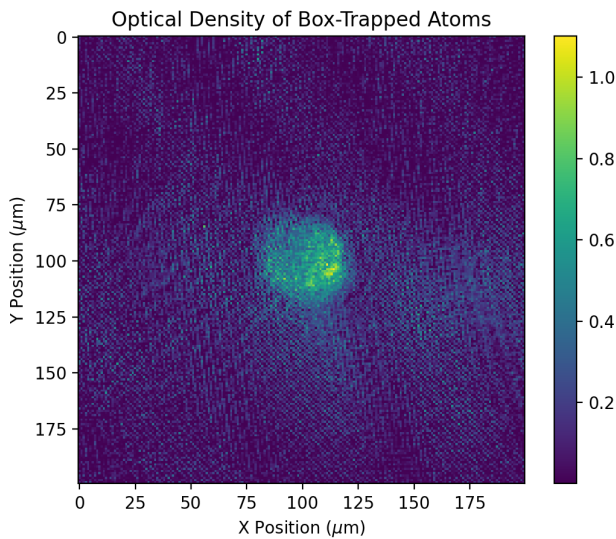


Figure 13: Absorption image of erbium atoms in a pancake trap. The faint outline of the trapping beam can be found in the ring of zero optical density around the atoms.

sible to implement a pancake trap containing atoms using the optimised tube trap we have discussed in Section 3 due to the long-term malfunctioning of the laser that powers the ODT transport beams. Nevertheless, this result of box-trapped atoms offers a promising proof-of-concept, helping us look forward to further tests on a fully-functioning erbium machine.

5 CONCLUSION

We have thus achieved optimisation of the optical setup and SLM hologram parameters to generate a box trap with a fitted power law exponent of 18.1, a trap depth of $2.15\mu\text{K}$ with angular uniformity range $\pm 23\%$, and a small, random floor noise averaging

$0.018\mu\text{K}$. The current trapping system generates a $0.19\mu\text{K}$ trap depth per 1mW of trapping beam incident on the SLM and is open to further optimisation.

The promising results of a proof-of-concept box trap containing 8,300 erbium atoms drive us to continue the full implementation of the pancake trap.

REFERENCES

- [1] L. Xu, J.-B. Yuan, S.-Q. Tang, W. Wu, Q.-S. Tan, and L.-M. Kuang, “Non-Markovian enhanced temperature sensing in a dipolar Bose-Einstein condensate,” *Phys. Rev. A*, vol. 108, no. 2, Aug. 2023, publisher: APS.
- [2] J. Wang, X.-J. Liu, and H. Hu, “Roton-Induced Bose Polaron in the Presence of Synthetic Spin-Orbit Coupling,” *Phys. Rev. Lett.*, vol. 123, no. 21, p. 213401, Nov. 2019, publisher: APS.
- [3] B. Butterfly, “Magneto-Optical Traps: from Quantum Computing to Redefining Time,” Mar. 2017.
- [4] L. Hofer, “Harnessing Machine Learning for the Analysis of Erbium Dipolar Quantum Gas Experiments,” 2023.
- [5] R. P. Smith, “Quantum Gases in Optical Boxes.”
- [6] M. Krstajic, “Experimental Platform for a Box-Trapped Dipolar Quantum Gas,” Jun. 2021.
- [7] A. L. Gaunt, “Degenerate Bose Gases: Tuning Interactions & Geometry,” Oct. 2014.
- [8] A. L. Gaunt, T. F. Schmidutz, I. Gotlibovych, R. P. Smith, and Z. Hadzibabic, “Bose-Einstein Condensation of Atoms in a Uniform Potential,” *Phys. Rev. Lett.*, vol. 110, no. 20, May 2013.
- [9] D. Ruttle, “Summer Project 2019 Summary,” Sep. 2019.
- [10] C. Foot, J., “Oxford Master Series in Atomic, Optical, and Laser Physics,” in *Atomic Physics*.